# Modelling thick-walled aluminium extrusions in side-crash applications

E. Teixidó-Marquès[1], D. Morin[1], O.S. Hopperstad[1], T. Berstad[1], B. Olsson[2], M. Costas[1]

[1] Structural Impact Laboratory (SIMLab), Department of Structural Engineering, Norwegian University of Science and Technology (NTNU), Trondheim, Norway
[2] Hydro Extruded Solutions AB, Finspång, Sweden

## Abstract

In this study, the numerical modelling of a thick-walled aluminium extrusion which serves as a protective structure for battery trays in electric vehicles was studied. The thick-walled profile was modelled in a pole-crushing test. For this application, four aluminium alloys of different strength were considered: AA6063, AA6082, AA6005 air-cooled and AA6005 water-cooled. Shell elements proved to be inadequate in accurately describing the mechanical behaviour of thick-walled extrusions. Differences in the deformation mode and the computed force were observed between shell and solid models. Parametric studies were performed to evaluate the effect of fracture model, element formulation, contact formulation, and friction coefficient.

## 1 Introduction

A critical consideration in the design of protective structures for electric vehicles is their energy absorption capacity. The development of lightweight structures is essential, as the range and weight of electric vehicles are intrinsically linked [1]. High-strength aluminium structures are frequently used due to their high strength-to-weight ratio and excellent ductility. Aluminium alloys within the 6xxx series are of significant interest due to their good performance in energy absorption applications when subjected to severe mechanical loads [2].

Traditionally, in the automotive sector, extruded profiles are modelled using shell elements, which are based on the plane stress assumption. This approach is generally accepted for thin-walled profiles [3]. In contrast, shell elements inadequately describe the mechanical behaviour of complex thick-walled structures. As the wall thickness becomes significant in relation to the other dimension of the extrusion, stresses and deformations appear in the thickness direction, which could lead to the formation of out-of-plane shear cracks. Therefore, the use of shell elements appears unsuitable for this application.

A comparison between solid and shell models in the simulation of a pole-crushing test on a thick-walled aluminium extrusion is presented. Parametric studies are conducted to investigate the effect on shear failure of the fracture criterion, the element formulation, the contact formulation and the friction coefficient applied to the modelling of a thick-walled structure.

## 2 Material calibration

### 2.1 Uniaxial tensile test

This work focuses on the numerical modelling of an aluminium extruded profile, which protects battery trays from a side crash. Fig 1 shows the extruded profile and the cross-section. The profile has a height of 148.6 mm and a width of 59.5 mm. The profile presents a multi-chamber design, with thicknesses varying from 3 mm to 6.5 mm. Four aluminium alloys within the 6xxx series were investigated for this profile: AA6063, AA6082, AA6005 air-cooled, and AA6005 water-cooled. All alloys were heat-treated to peak strength condition (temper T6).

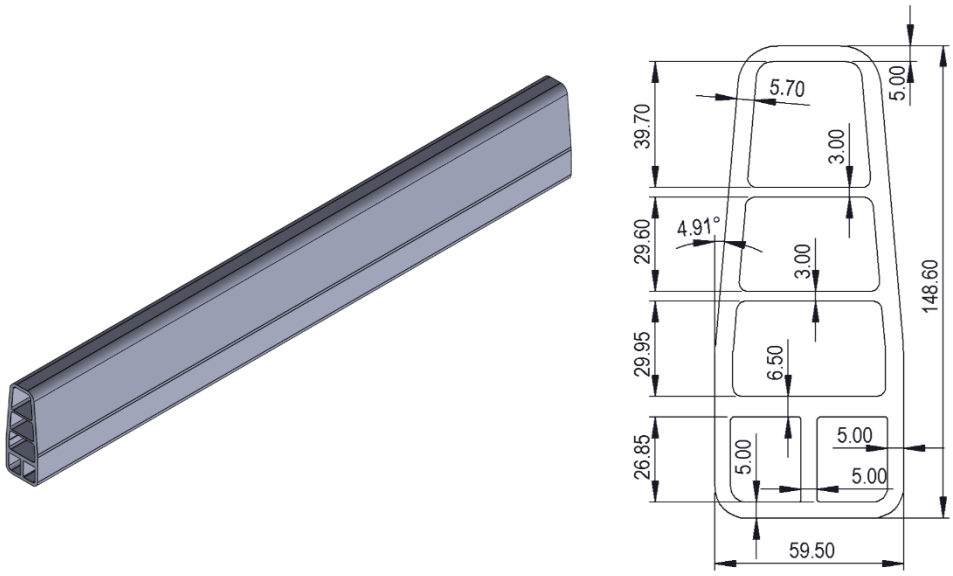


(a) (b)

*Fig.1: Illustration of (a) the extruded profile and (b) the cross-section (dimensions in mm).*

Material properties for each alloy were obtained from a tensile test. Uniaxial tensile tests were conducted in a universal testing machine, with a constant crosshead velocity corresponding to an approximate initial strain rate of $2.5 \cdot 10^{-4}\ s^{-1}$. A 50 mm extensometer was used to calculate the engineering strain. The experimental engineering stress-strain curves are shown in Fig.2.

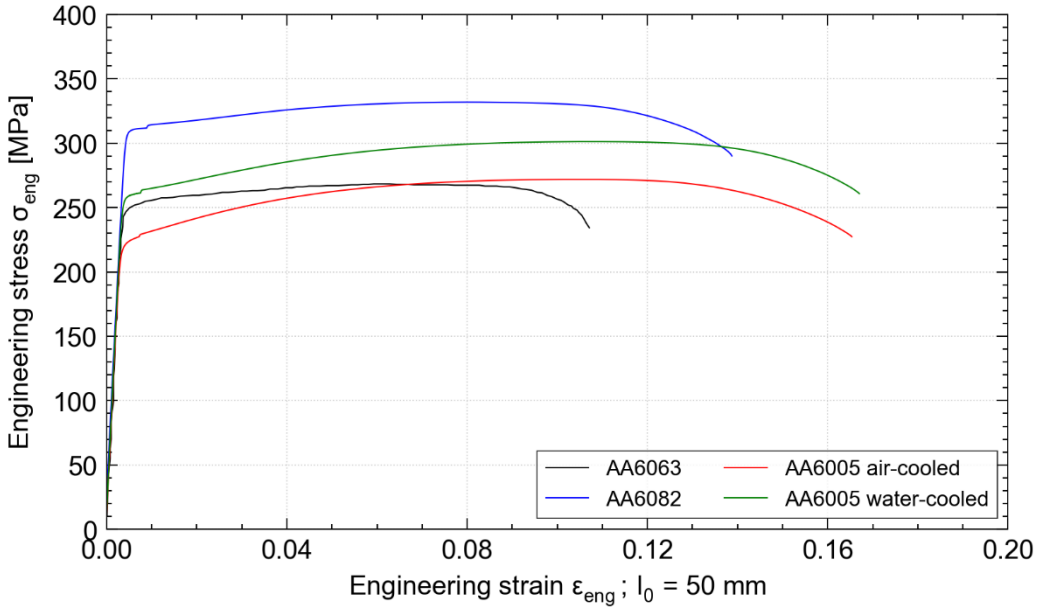


*Fig.2: Experimental engineering stress-strain curves.*

The specimen geometry used in the uniaxial tensile test is shown in Fig.3.

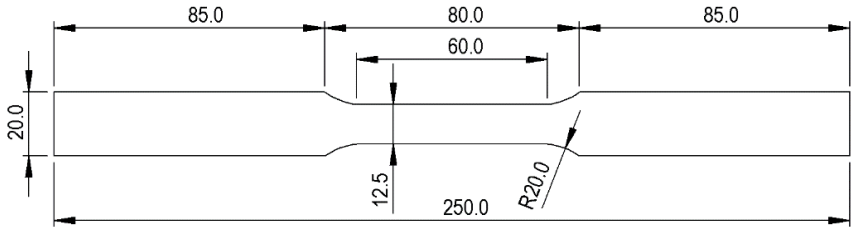


*Fig.3: Geometry of the UT specimens (dimensions in mm).*

### 2.2 Material modelling

For simplicity, the different aluminium alloys were considered to be isotropic. This approach led to a significant reduction in the computational cost compared to using an anisotropic material model. A hypo-elastic plastic material model was assumed to describe the material behaviour.

The elastic modulus and the Poisson's ratio were assumed to be $\mathrm{E} = 70\ \mathrm{GPa}$ and $\nu = 0.3$, respectively. The yield function can be expressed in the following terms

$$f = \sigma_{\mathrm{eq}} - (\sigma_0 + R) \leq 0, \tag{1}$$

where $\sigma_{\mathrm{eq}}$ is the equivalent stress, $\sigma_0$ is the initial yield stress and $R$ represents the isotropic work-hardening.
The equivalent stress is calculated using the Hershey-Hosford yield criterion, defined as

$$\sigma_{\mathrm{eq}} = \left[\frac{1}{2}(|\sigma_I - \sigma_{II}|^m + |\sigma_{II} - \sigma_{III}|^m + |\sigma_I - \sigma_{III}|^m)\right]^{\frac{1}{m}}, \tag{2}$$

where $\sigma_I \geq \sigma_{II} \geq \sigma_{III}$ are the principal stresses and $m$ defines the shape of the yield surface. A value of $m = 8$ is chosen as it is the recommended value for aluminium alloys [4].

The isotropic work-hardening was defined by a two-term Voce law as described by

$$R = \sum_{i=1}^{2} Q_i \left[1 - \exp\left(-\frac{\theta_i}{Q_i}\, p\right)\right], \tag{3}$$

where $Q_i$ define the saturation stresses, $\theta_i$ express the initial word-hardening moduli, and $p$ is the equivalent plastic strain.

In this work, the influence of the damage model on the shear ductility is studied. An uncoupled ductile failure criterion is applied to model damage. The Extended Cockcroft-Latham (ECL) damage criterion [5] was adopted to predict material failure. The ECL damage indicator defines damage according to

$$D = \frac{1}{W_{\mathrm{c}}} \int \sigma_{\mathrm{eq}} \left\langle \phi \frac{\sigma_I}{\sigma_{\mathrm{eq}}} + (1 - \phi)\left(\frac{\sigma_I - \sigma_{III}}{\sigma_{\mathrm{eq}}}\right)\right\rangle^{\gamma} \mathrm{d}p, \tag{4}$$

where $D$ is the damage variable, $\sigma_{\mathrm{eq}}$ is the equivalent stress, $W_{\mathrm{c}}$ defines the ductility of the material, $\sigma_I$ and $\sigma_{III}$ are the major and minor principal stresses, respectively, $\phi$ governs the influence of the major principal stress and the maximum shear stress, $\gamma$ controls the strength of the stress-state dependence, and $p$ is the equivalent plastic strain. The Macaulay bracket $\langle\cdot\rangle$ represents $\langle x\rangle = \max(x, 0)$. Failure occurs when the damage parameter $D$ reaches a value of 1 at an integration point.

Setting $\phi = \gamma = 1$ yields to the Cockcroft-Latham (CL) damage criterion

$$D = \frac{1}{W_{\mathrm{c}}} \int \langle \sigma_I \rangle \ \mathrm{d}p. \tag{5}$$

The CL criterion is a simple failure criterion that can be calibrated from a tensile test, thus reducing the number of material tests to calibrate the damage model.

### 2.3 Material calibration

An inverse modelling approach was used to calibrate the material model. LS-OPT® was employed to fit the work-hardening parameters from a uniaxial tensile test. A solid element model of a tensile test was simulated in LS-DYNA R15.0.2. A representative engineering stress-strain curve obtained from a uniaxial test was used for each aluminium alloy as the target curve to calibrate the $Q_i$ and $\theta_i$ parameters from the work-hardening rule.

The numerical tensile tests were modelled using 1/8 of the tensile specimen geometry and three symmetry planes, as shown in Fig.4. Ten solid elements were used to model the tensile specimen thickness, leading to a solid element size of 0.55 mm. Solid elements were modelled using the default formulation ELFORM = 1, and an hourglass control IHQ = 5 with QM = 0.03 was applied.

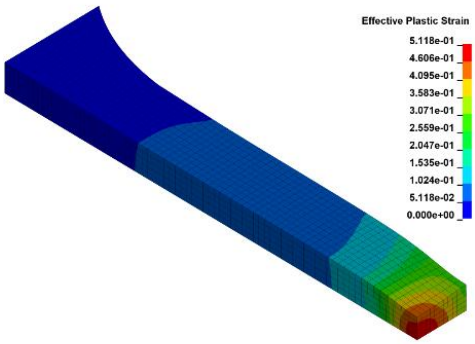


*Fig.4: Fringe plot of the effective plastic strain of the UT specimen adopted for material calibration.*

The material card ***MAT_33** was used to model the material behaviour. The anisotropic coefficients were set to unity, i.e. $A = B = C = D = E = F = G = H = 1$, to account for an isotropic behaviour. The parameter $M$ was set equal to 8, thus defining the Hershey-Hosford yield surface for FCC alloys.

The inverse model was used to calibrate the failure criterion for each material. The CL criterion was adopted to calibrate the critical value $W_c$. The ECL was later applied to study the influence of $\phi$ on the damage model.

The inverse model was run until the engineering strain of a virtual extensometer matched the engineering strain at failure from the experimental test. The major principal stress $\sigma_I$ and the equivalent plastic strain $p$ at the centremost element from the numerical tensile test were computed. The failure parameter $W_c$ was obtained by integrating the major principal stress $\sigma_I$ over the equivalent plastic strain $p$ up to the equivalent plastic strain at which failure occurs, as

$$W_c = \int_0^{p_f} \langle \sigma_I \rangle \, \mathrm{d}p, \tag{6}$$

where $p_f$ is the equivalent plastic strain at failure.

The engineering stress-strain curves from the experimental tests and the numerical calibrations are shown in Fig.5.

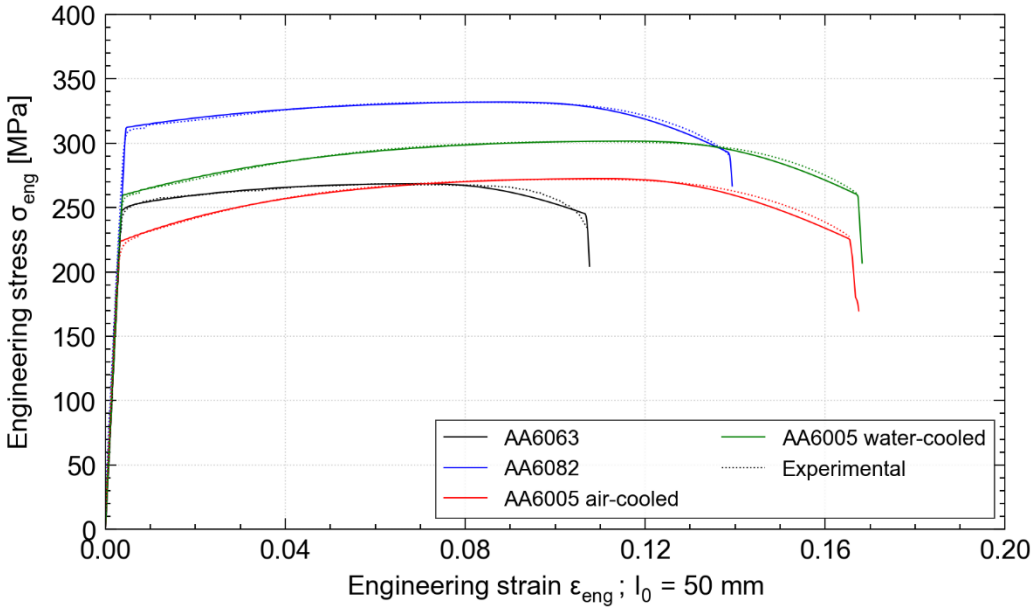


*Fig.5: Experimental and numerical engineering stress-strain curves.*

The calibrated parameters for the Voce work-hardening law and the CL criterion are compiled in Table 1.

| Alloy | $\sigma_0$ | $\theta_1$ | $Q_1$ | $\theta_2$ | $Q_2$ | $W_c$ |
|---|---|---|---|---|---|---|
| **AA6063** | 247.8 | 3183 | 3.730 | 941.8 | 51.36 | 110.5 |
| **AA6082** | 311.0 | 90440 | 2.000 | 892.1 | 82.23 | 202.4 |
| **AA6005 air-cooled** | 224.0 | 1328 | 91.20 | 345.3 | 8.074 | 214.7 |
| **AA6005 water-cooled** | 260.0 | 1303 | 103.7 | 0 | 917.6 | 209.3 |

*Table 1: Parameters of the Voce work-hardening rule and CL criterion, given in MPa.*

## 3 Numerical simulations

### 3.1 Model description

Fig.6 shows the set-up and the finite element model representing a pole-crushing test on a thick-walled aluminium extrusion. A cylindrical punch with a diameter of 60 mm was used to simulate a lateral impact. Both the punch and the fixed wall were modelled as rigid parts.

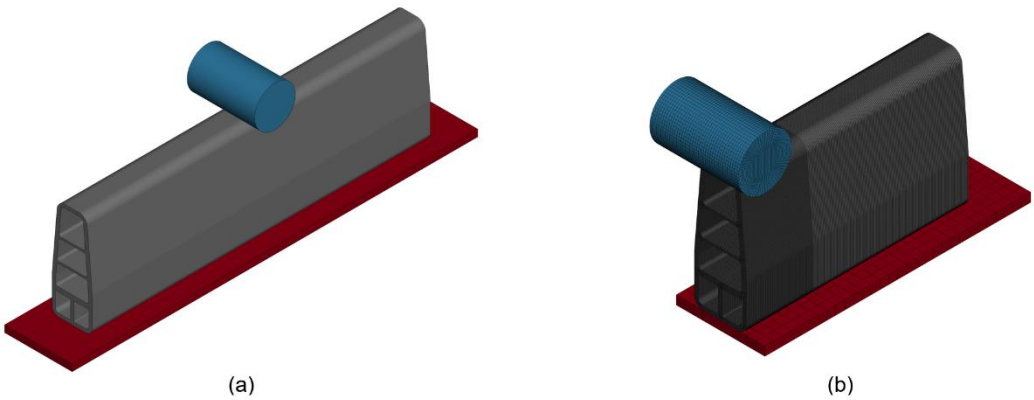


*Fig.6: (a) CAD representation of the pole-crushing test set-up and (b) finite element model with a symmetry plane.*

Different numerical models were run in this work. First, a solid model without damage was adopted to compare the influence of the material on the mechanical behaviour of the profile. A solid model with a damage criterion was later employed to study the effect of damage on each alloy. A comparison between shell and solid models was conducted to analyse the differences in both techniques when modelling a thick-walled profile. Lastly, solid models were used to perform different parametric studies. The influence of the damage model on the shear ductility, the contact formulation, the element formulation and the friction coefficient were analysed.

Material properties for each aluminium alloy were adopted from results obtained in Section 2.3. Different material models were used in this work. For models in which damage was neglected, ***MAT_33** was applied. Alternatively, for simulations in which damage was considered, a ***MAT_USER_DEFINED_MATERIAL_MODELS** was adopted.

As it can be observed from Fig.6b, two different element sizes were adopted for the solid models. A refined mesh was used in regions that exhibited large plastic deformations. A coarser mesh was employed for the remaining regions of the profile to reduce the computational cost of the numerical model.

Quasi-static tests were simulated. A time-scaling factor was applied to reduce the computational cost. Computational time was also reduced by modelling one-half of the extrusion due to the presence of a symmetry plane. Quasi-static conditions were ensured by checking that the kinetic energy was negligible compared to the internal energy. The simulation was terminated once a punch displacement of 90 mm was reached.

All degrees of freedom corresponding to the fixed wall were constrained. Regarding the cylindrical actuator, rotations and displacements were constrained except for the displacement corresponding to a vertical direction. The actuator was initially placed 0.5 mm above the aluminium extrusion to avoid initial mesh penetrations. A ***DEFINE_CURVE_SMOOTH** was employed to define the velocity of the actuator to avoid numerical instabilities.

### 3.2 Solid Model

The mechanical behaviour of the thick-walled profile for each aluminium alloy was first modelled using solid elements. A mesh with an element size of 0.55 mm was used. The default solid element formulation ELFORM = 1 was used. An hourglass control IHQ = 5 and QM = 0.03 was applied to avoid hourglass deformation modes.

#### *3.2.1 Numerical simulations without damage*

Initially, damage was not considered. Material properties for each aluminium alloy were defined in ***MAT_33**. All anisotropic coefficients were set to 1 in order to describe isotropic behaviour.

Contact between rigid parts and the aluminium specimen was modelled by applying ***CONTACT_AUTOMATIC_SURFACE_TO_SURFACE** with SOFT = 1. To model the specimen's self-contact, ***CONTACT_AUTOMATIC_SINGLE_SURFACE** with SOFT = 1 was used. In all contacts, a friction coefficient equal to 0.3 was defined for static and dynamic friction coefficients.

Fig.7 shows the force-displacement curves for each aluminium alloy without damage. As it can be observed, the force curves show similar overall behaviour, although different force values are computed for each aluminium alloy. Results shown in Fig.7 are in agreement with the results obtained from the uniaxial tensile test in Fig.5. Aluminium alloy AA6082 was found to be the strongest material, followed by AA6005 water-cooled. AA6063 turned out to be the softest material. A maximum difference of 150 kN was observed between the force levels for AA6082 and AA6063.

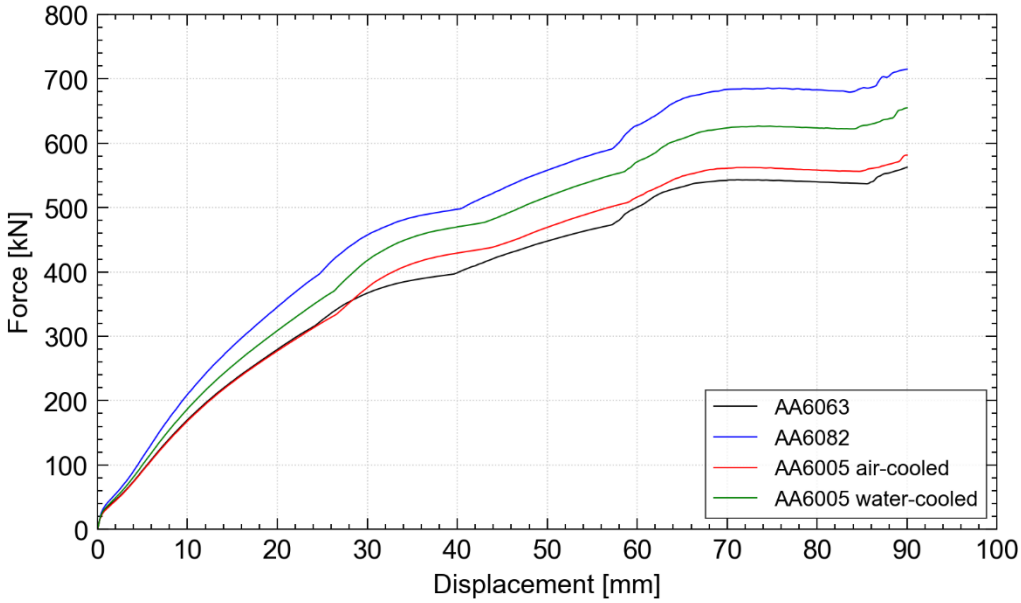


*Fig.7: Force-displacement curves obtained from a pole crushing test for different aluminium alloys. A damage model was not applied in the numerical simulations.*

All materials showed a similar deformation behaviour. As depicted in Fig.8, fringe plots of the effective plastic strain show that the maximum plastic strains are concentrated in the corners of the top wall. Therefore, failure is expected to be initiated in those regions for models in which a damage model is introduced.

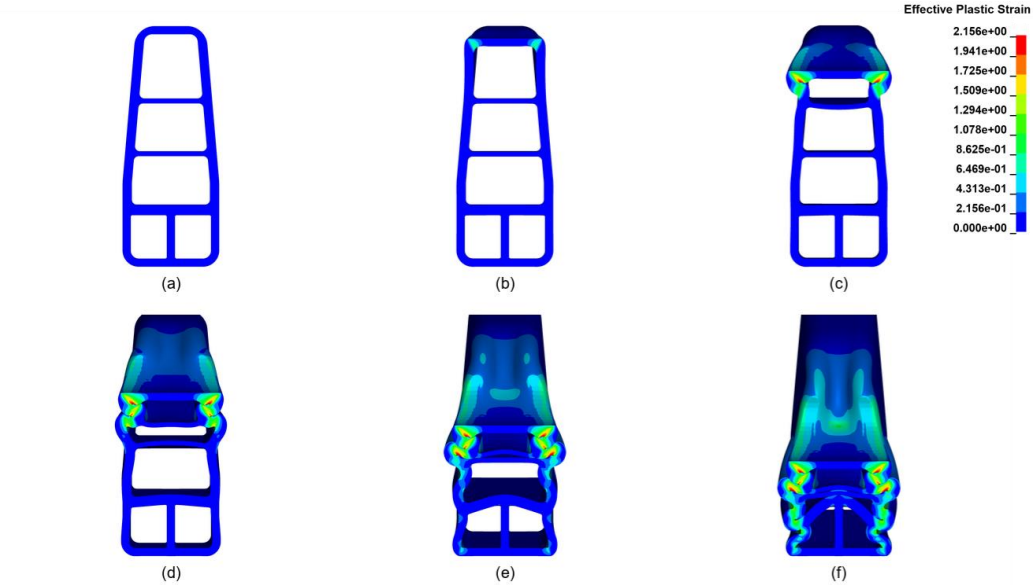


*Fig.8: Fringe plots of the effective plastic strain.*

### *3.2.2 Numerical simulations with the Cockcroft-Latham criterion*

To include a damage model in a crushing pole test, a ***MAT_USER_DEFINED_MATERIAL_MODELS** material model was used. The CL criterion was adopted by setting $\phi$ and $\gamma$ equal to 1. Also, the critical damage parameter $W_c$ was defined for each aluminium alloy to its corresponding value found in Section 2.3.

As failure occurs in the form of element erosion, ***CONTACT_ERODING_SURFACE_TO_SURFACE** was used to model contact between rigid parts and the thick-walled aluminium extrusion. Similarly, ***CONTACT_ERODING_SINGLE_SURFACE** was adopted to account for self-contact. ***ERODING** contacts were preferred as they update the contact surface and reduce element penetration.

The force-displacement curves are depicted in Fig.9. It can be observed that all aluminium materials except for AA6005 air-cooled exhibit a drop of force at some point of the test, which is associated with material failure. Although AA6005 air-cooled does not show a force drop, the initiation of a transverse fracture was observed at the later stages of the simulation.

In good agreement with the results shown in Fig.5, AA6063 fails first. Also, AA6063 is the aluminium alloy to fail at the lowest force value, just over 300 kN. AA6082 is the material which exhibited the highest force values before damage occurred. For this alloy, fracture is predicted to happen at 46 mm and at a force of 520 kN. By contrast, the formation of a crack is delayed for the AA6005 water-cooled alloy. As in Fig.5 this alloy showed to have high ductility, material failure is found to occur at 73 mm. However, the force drop does not occur in a sudden manner, contrary to what is observed for the other alloys. Instead, a minor force drop is observed when the fracture initiates, followed by a later major force drop related to the propagation of the crack.

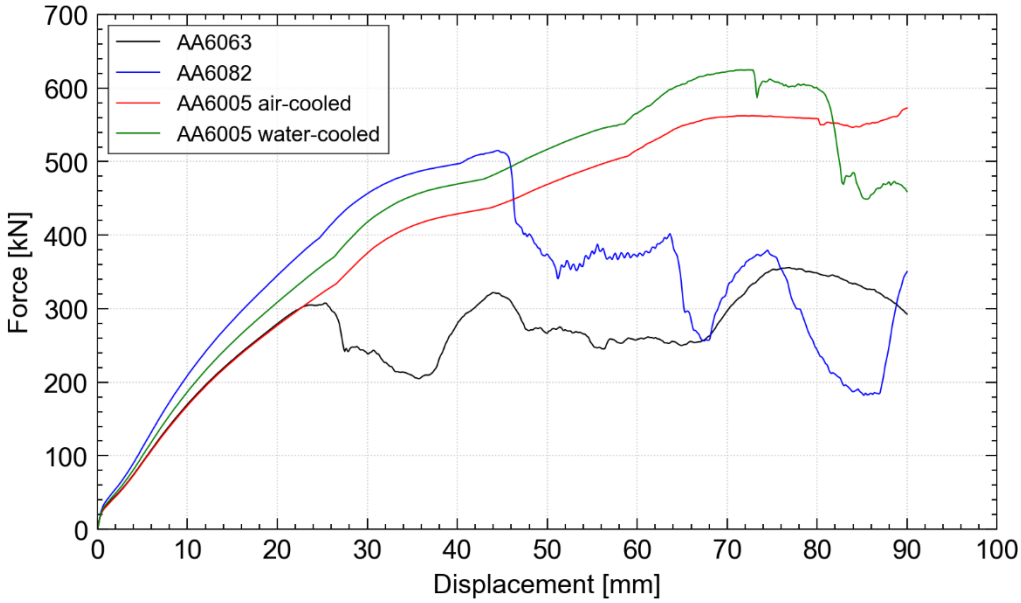


*Fig.9: Force-displacement curves obtained from a pole crushing test for different aluminium alloys using the CL damage model.*

Two different types of fracture are observed in Fig.10. The AA6063 alloy shows failure caused by a crack formed at the top corners of the profile. This fracture is observed to propagate across the thickness. The other aluminium alloys fail by the formation a transverse crack occurring on the top wall of the profile. This crack is observed to initiate on both sides of the outer surface of the top wall, caused mainly by excessive tension. A rapid fracture propagation is observed due to a secondary crack initiating on the middle of the top wall for the AA6082 alloy. A different behaviour is observed for the AA6063 water-cooled alloy. The formation of this secondary crack occurs at a later stage, leading to a slower fracture propagation and consequently, delaying the force drop observed in Fig.9. Regarding the AA6063 air-cooled alloy, the first crack originates in the middle of the top wall, whereas a second crack is initiated on the sides of the top wall. However, both cracks do not merge for the applied displacement.

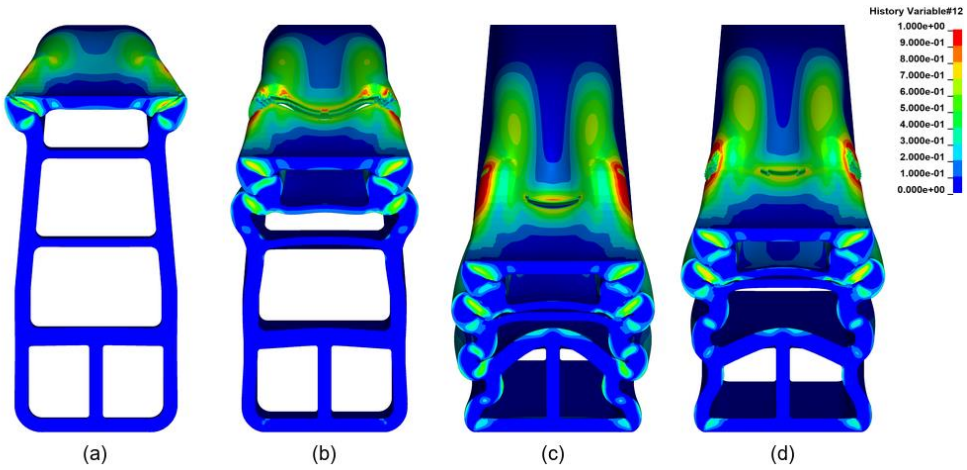


*Fig.10: Fringe plots of the damage variable $D$. Pictures correspond to the deformation frame in which the first crack was observed for each aluminium alloy. (a) AA6063 (b) AA6082 (c) AA6005 air-cooled and (d) AA6005 water-cooled.*

### 3.3 Shells vs solids

A comparison between shells and solids was conducted. The goal was to quantify the differences between shells and solids when modelling thick-walled profiles.

An element size of 5 mm was employed for the shell model, leading to $\frac{l_e}{t_e} \approx 1$, where $l_e$ is the element size and $t_e$ is the element thickness. Two different shell formulations were adopted. The default shell formulation ELFORM = 2 was combined with an hourglass control IHQ = 4 and QM = 0.03. The shell formulation ELFORM = 16 was also used together with hourglass control IHQ = 8. For both formulations, NIP = 5 was defined. Drilling stiffness was included later in both models to analyse its influence over a shell model.

To compare both shell and solid models, only material properties from AA6082 were considered. ***MAT_258** material model was adopted for the shell model. This material model was preferred as it proved to work properly for thin-walled aluminium extrusions [6].

#### *3.3.1 Shells vs solids without damage*

First, a comparison between shells and solid models without considering damage was conducted. Although ***MAT_258** includes a failure criterion, it was disabled by setting the critical damage value DCRIT to a large number. The solid model and the contacts used for both shell and solid models were defined as described in Section 3.2.1.

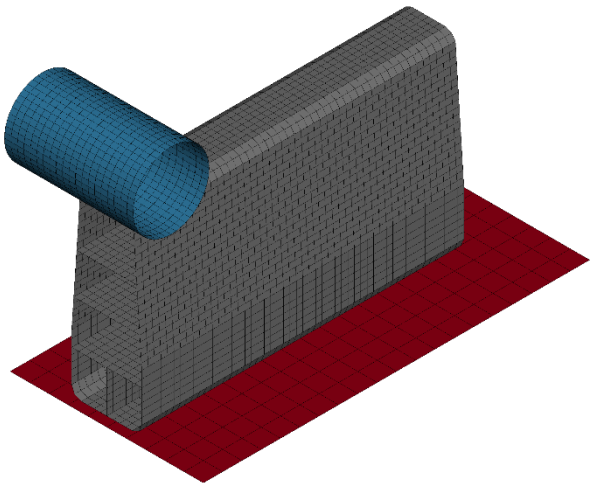

*Fig.11: Shell finite element model of the pole crushing.*

The force-displacement curves are shown in Fig.12. A clear difference can be observed between the shell and solid models. Although initially the shell and solid models display similar force values, lower values of force are exhibited by the shell models after a 10 mm displacement value. The shell models show similar curves, which are significantly different from the solid model. This difference is mainly related to the deformation mode shown in Fig.13. The use of the default shell element ELFORM = 2 resulted in the lowest force curve. Slightly higher forces were obtained by ELFORM=16. On average, an offset of 12 kN is obtained between the two curves.

Applying a drilling stiffness has some effects in models with ELFORM = 2. Fig.12 reveals that similar forces as in EFORM = 16 are computed for ELFORM = 2 when a drilling stiffness is applied. On the other hand, the effect of the drilling stiffness in ELFORM = 16 is marginal, as minor changes in force values are obtained.

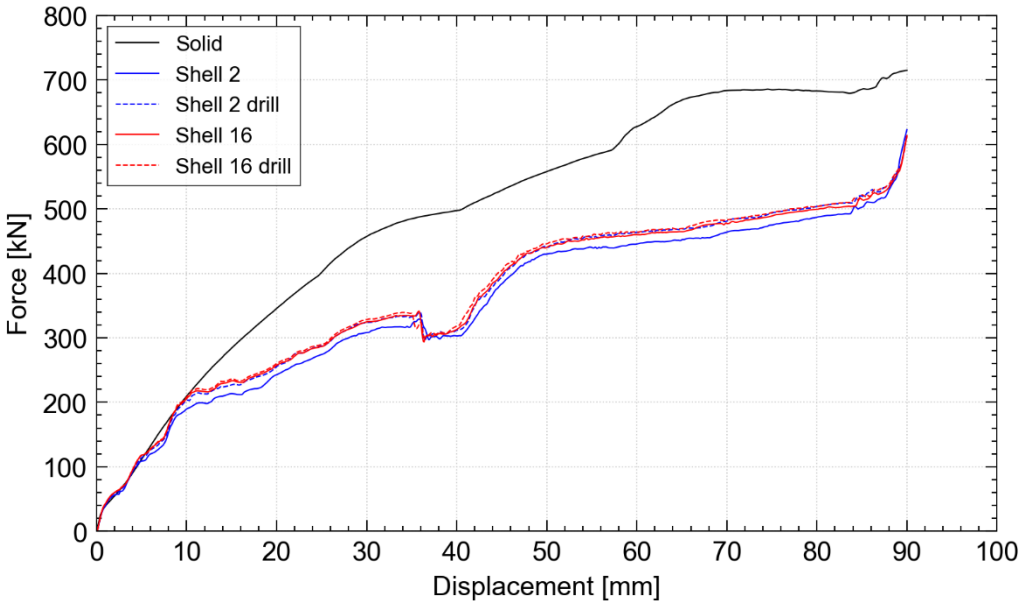


*Fig.12: Force-displacement curves for the shell and solid models without damage.*

Differences between solid and shell elements are also observed in the deformation mode, as depicted in Fig.13. The solid model shows a downward bending for the second horizontal wall. In contrast, the shell model exhibits the opposite deformation, as the second wall bends upwards. The bending direction of this wall is critical, as it drives the deformation of the consecutive walls. A downward bending is followed by outward buckling of the sidewalls, as seen in the solid model. On the contrary, the shell model shows that an upward bending of the horizontal wall causes an inward buckling on the sidewalls.

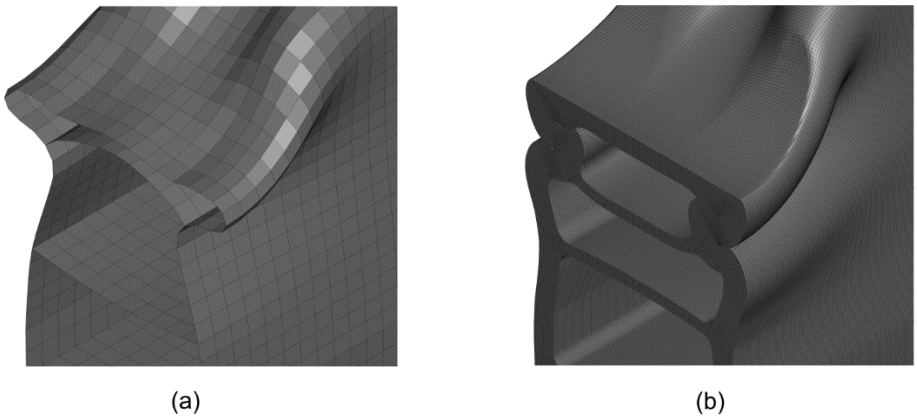


*Fig.13: Deformation for the (a) shell and (b) solid models.*

### *3.3.2 Shells vs solids with the Cockcroft-Latham criterion*

A second comparison between shells and solids was performed. The CL damage criterion was included in both shells and solids models.

Damage was included for shell models by setting DCRIT = 1, WCB = WCL = WCS and CC = 0 in ***MAT_258**. The calibration of these parameters was conducted following the procedure described in [6]. The solid model was modelled as defined in section 3.2.2.

Fig.14 shows the force-displacement curves for shell and solid models with a damage model. A similar behaviour as in Fig.12 is found when damage is applied. The solid model exhibits a higher force curve compared to shell models, while shell models compute similar force curves. From Fig.14, it can be observed that the shell models predict an early failure compared to the solid model. Depending on the ELFORM applied, the shell models exhibit a force drop related to material failure between 30 mm to 40 mm of displacement. By contrast, this force drop is delayed until 46 mm of displacement is reached for the solid model.

Similarly to Fig.12, the shell model with ELFORM = 2 exhibits lower forces compared to ELFORM = 16. Furthermore, this type of element is the earliest to predict failure. ELFORM = 16 results in higher computed forces, and a later prediction of failure. Shell models with ELFORM = 16 are insensitive to the application of a drilling stiffness. Failure is predicted at a similar displacement and the force curve shows minor changes when a drilling stiffness is defined. On the other hand, applying a drilling stiffness on ELFORM = 2 leads to higher force values. As it can be observed in Fig 14, the force-displacement curve resembles the force curves presented by ELFORM = 16. However, failure is predicted at a later stage, as the force drop is observed to occur around 40 mm of displacement.

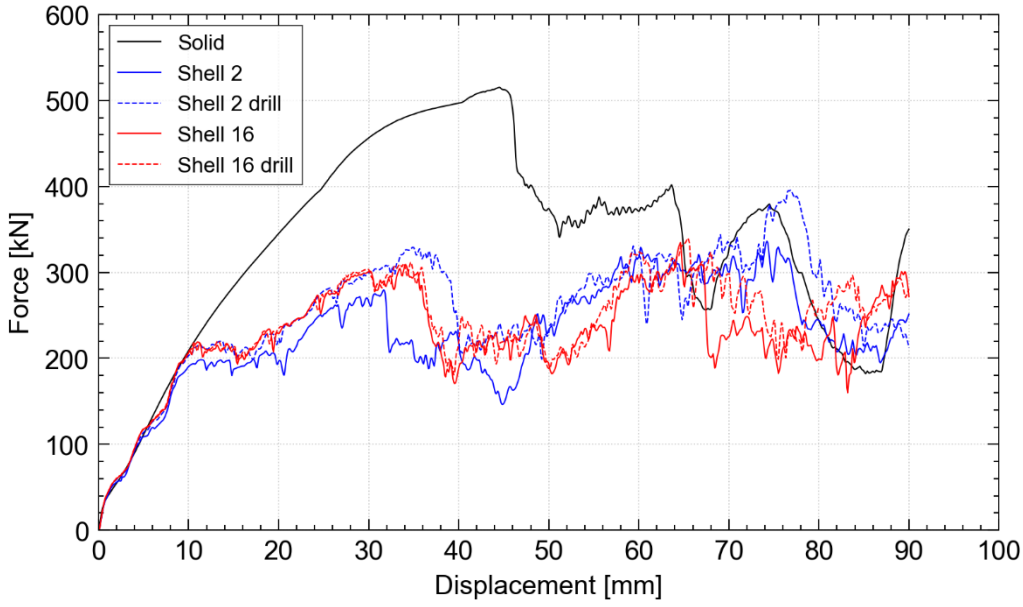


*Fig.14: Force-displacement curves for the shell and solid models with the CL criterion.*

Shell models exhibit an early failure compared with the solid model. A first crack is observed at a displacement of 13 mm. This crack occurs at the top corners of the profile and propagates along the extrusion direction. A second crack is observed to initiate at the sides of the top wall after a displacement of 29.5 mm is reached. A major force drop is observed mainly caused by the merging of the two cracks.

The solid model shows a different behaviour compared to the shell models. A first crack is observed on the outer surface of the top wall, followed by a second crack initiating in the middle of the top wall. Compared to shells, failure is delayed to a displacement of 46 mm after both cracks propagate and join to form a major crack.

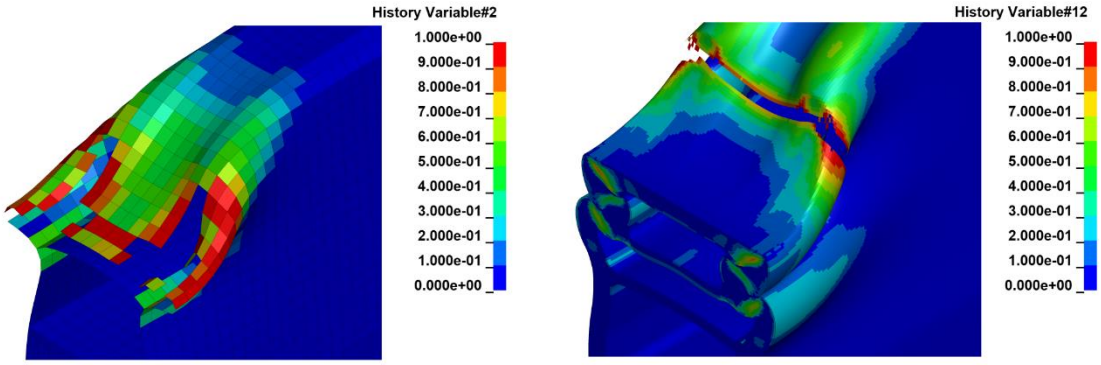


(a) (b)

*Fig.15: Fringe plots of the damage variable $D$ for (a) shell and (b) solid models.*

### 3.4 Parametric study

A parametric study was conducted to evaluate the parameters of the damage model, the element formulation, the contact defined between parts and the friction coefficient. The parametric study was conducted for a single material. Aluminium alloy AA6082 was chosen as the most representative material.

Regarding the damage model adopted, the ECL model was now applied. This damage model offers greater flexibility as it accounts for the shear ductility in the damage formulation. Shear failure modes can be enabled by controlling the parameter $\phi$. Therefore, different types of failure were observed by varying the damage model parameter $\phi$.

#### *3.4.1 Influence of the shear ductility*

The ECL model parameter $\phi$ was varied from 1 to 0, whereas the parameter $\gamma$ was set to 1 for all cases. The failure parameter $W_c$ from Table 1 for the AA6082 was used. Material properties were defined by ***MAT_USER_DEFINED_MATERIAL_MODELS**. Same element size, element formulation and contact formulation as described in section 3.2.2 were adopted

Fig.16 compares force-displacement curves for different values of $\phi$. It can be observed that a lower value of $\phi$ causes earlier fracture. When the CL criterion is applied, meaning $\phi = 1$, fracture occurs at a force above 500 kN and a displacement of 46 mm. When $\phi$ is reduced to 0.75, the first drop of force occurs close to 300 kN, and failure appears at 16 mm of displacement. Setting $\phi$ to a value of 0.5 leads to an earlier first crack. In this case, fracture appears at a displacement of 10 mm, which corresponds to a force of 200 kN. As shown in the figure, fracture appears before the 10 mm of displacement for values of $\phi$ lower than 0.5.

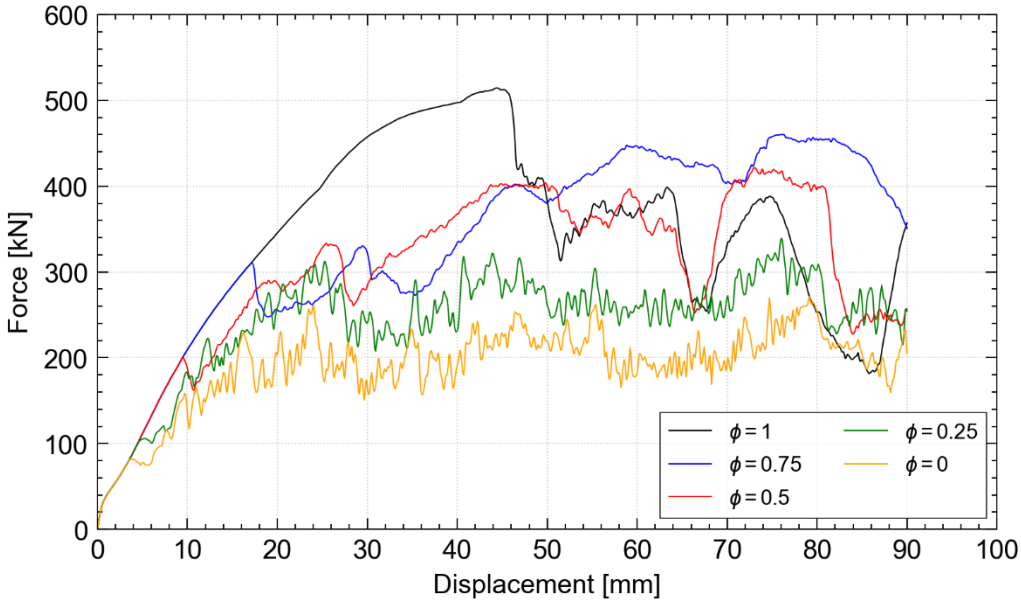


*Fig.16: Force-displacement curves for different $\phi$ values.*

Comparing the fringe plots of damage in Fig.17, two different types of fracture behaviour can be observed. For $\phi$ equal to 1, failure occurs by a transverse fracture caused by bending of the top wall of the profile, as observed in Fig.17a. However, reducing the value of $\phi$ leads to a different failure mode. It can be seen in Fig.17b and Fig.17c that fracture is initiated in the corners of the profile and appears in the thickness direction. This type of fracture is related to a shear-dominated deformation. These results indicate that the $\phi$ parameter plays a major role in the fracture mode for thick-walled extrusions, and proper calibration is necessary to obtain similar results as in experiments.

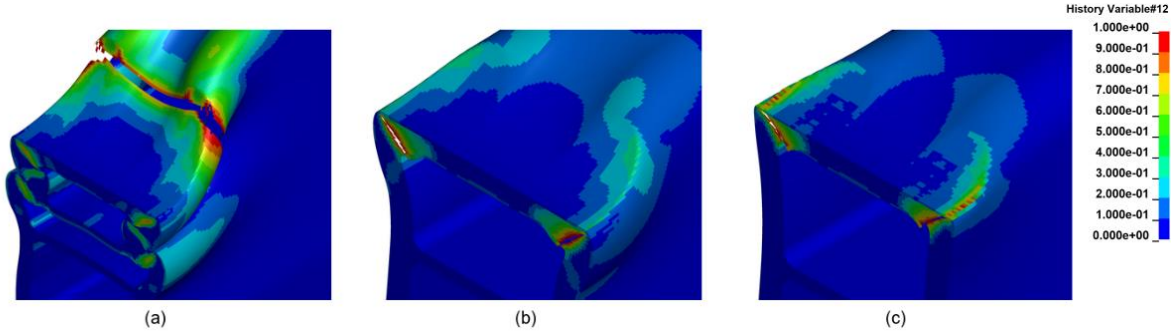


*Fig.17: Fringe plots of the damage variable $D$ for (a) $\phi = 1$, (b) $\phi = 0.75$ and (c) $\phi = 0.5$.*

### *3.4.2 Element formulations*

Different solid element formulations were used in the solid model of the pole crushing test. The following element formulations were considered:

- ELFORM = 1: Constant stress solid element
- ELFORM = 2: Selectively reduced 8-point hexahedron element
- ELFORM = -2: Selectively reduced 8-point hexahedron for poor aspect ratios
- ELFORM = 3: Fully integrated quadratic 8-node element with nodal rotations
- ELFORM = 23: 20-node hexahedron with reduced integration

Different mesh sizes were applied depending on the element formulation used. A refined mesh was employed for element formulation ELFORM = 1. This refined mesh was designed with a characteristic element length of 0.55 mm. A coarser mesh was adopted for the remaining element formulations. In these models, the elements had an approximate characteristic length of 1.25 mm. Finally, a one-element through-thickness mesh was also used to study the effectiveness of ELFORM = 23.

Material failure was turned off in this study. The ECL criterion has a strong dependency on the element size. Therefore, as different element sizes were employed in this analysis, ***MAT_33** was applied to model the material behaviour. Isotropic behaviour was assumed by setting the anisotropic coefficients to unity. A value M = 8 was applied to the yield surface exponent.

A ***CONTACT_AUTOMATIC_SURFACE_TO_SURFACE** with SOFT = 1 was used to model the contact between the rigid parts and the aluminium profile, while ***CONTACT_AUTOMATIC_SINGLE_SURFACE** with SOFT = 1 was used to account for the specimen self-contact. Friction was enabled by setting FD = FS = 0.3 in all contact formulations.

The hourglass control IHQ = 5 with QM = 0.03 was used for models with reduced integration solid element formulations, i.e. ELFORM = 1 and ELFORM = 23.

Numerical simulations modelled with ELFORM = 2 and ELFORM = -2 were found to be inappropriate for this type of application. A negative volume was computed in highly distorted elements, leading to the termination of the numerical simulation. The remaining element formulations succeeded in describing the deformation of the aluminium profile.

Fig.18 shows the force-displacement curves for the different element formulations. As it can be seen from the figure, two different force-displacement behaviours can be distinguished. The refined model with ELFORM = 1 and the coarse model with ELFORM = 23 give about the same force-displacement curve. On the other hand, the coarse mesh model with ELFORM = 3 and the one-element through-thickness mesh with ELFORM = 23 give a different behaviour. The four models exhibit a similar response for the first 25 mm of displacement, reaching a force value of 400 kN. From that stage, the refined mesh with ELFORM = 1 and the coarse model with ELFORM = 23 display higher forces compared to the other two models. By contrast, ELFORM = 3 and ELFORM = 23 with a one-element through-thickness mesh, experience a sudden increase of force at the later stages of the simulations due to a densification phenomenon.

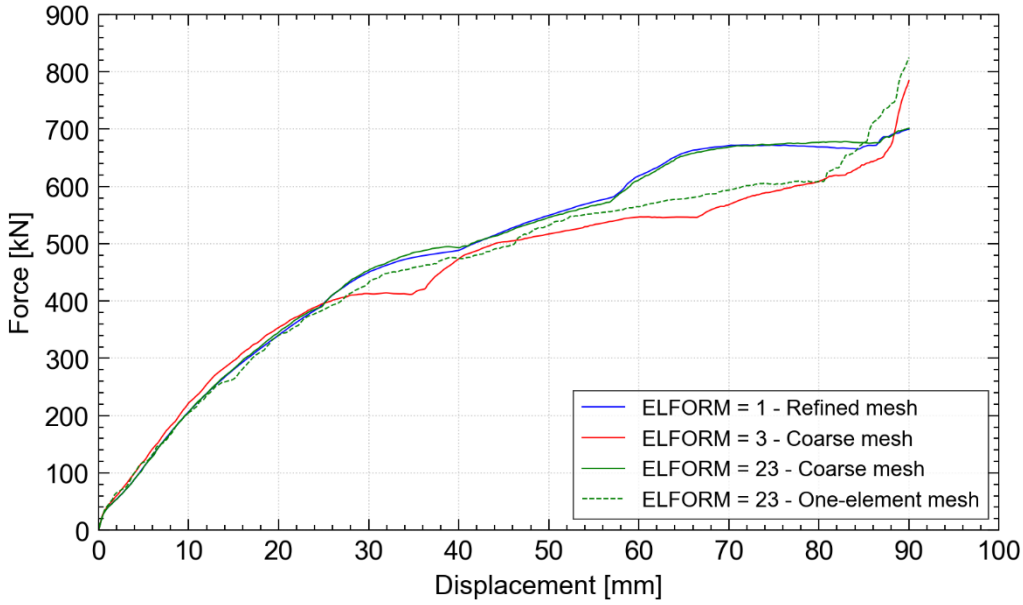


*Fig.18: Force-displacement curves for different element formulations.*

This difference in the force-displacement curve is associated with the deformation pattern observed in Fig.19. Initially, the four models capture the deformation of the top wall in a similar manner. However, a difference in the deformation of the second horizontal wall is observed. For ELFORM = 1 and the coarse model with ELFORM = 23, this wall bends downwards, whereas an upward bending can be noticed in the two other models. A large deformation at the corners of the profile is caused by a downward bending, thus leading to a higher exerted force caused by the contact of the surfaces. By contrast, there is less contact between surfaces for an inward bending mode. However, this deformation mode leads to a densification of the profile at the end of the test, which translates to an abrupt increase in force, as shown in Fig.18.

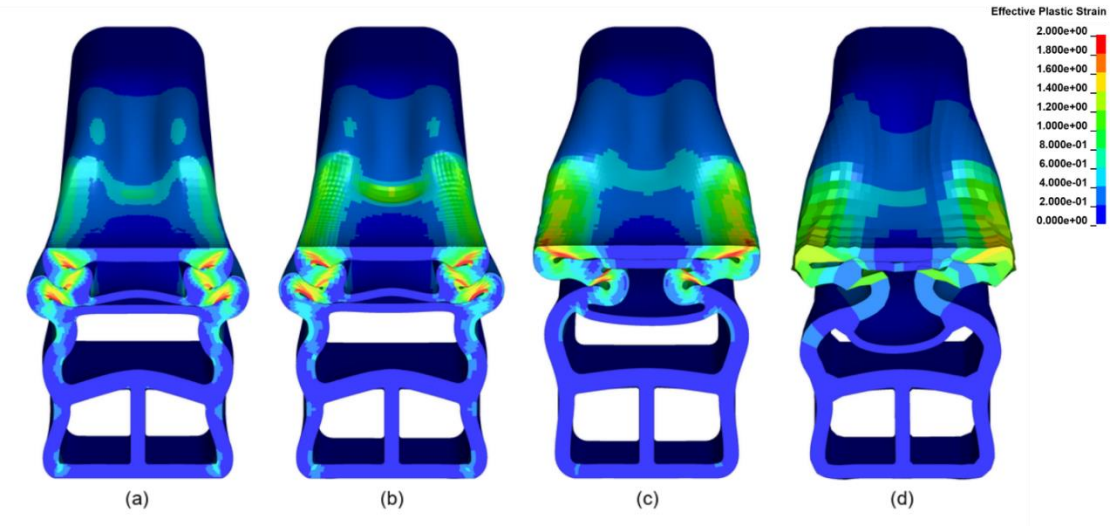


*Fig.19: Fringe plots of the effective plastic strain. (a) ELFORM = 1 – refined mesh (b) ELFORM = 23 – coarse mesh (c) ELFORM = 3 – coarse mesh (d) ELFORM = 23 - one-element through-thickness mesh.*

Table 2 illustrates the computational cost of each model. It can be seen from the data that a model with element formulation ELFORM = 23 and one-element through-thickness mesh is the least computationally expensive model. By contrast, the same element formulation but with a coarse mesh gives the highest computational time. Applying element formulation ELFORM = 1 for a refined mesh leads to the same force-displacement curve, as seen in Fig.18, for a lower computational cost.

| Model | CPU Time (hours) |
|---|---|
| ELFORM = 1 – Refined mesh | 8.10 |
| ELFORM = 3 – Coarse mesh | 3.55 |
| ELFORM = 23 – Coarse mesh | 16.78 |
| ELFORM = 23 – One-element through-thickness mesh | 0.22 |

*Table 2: Computational cost of element formulations. Models were simulated with 32 MPP processors.*

### *3.4.3 Contact formulations*

A set of contact formulations was applied to model the contact between the rigid parts and the aluminium extrusion. The following contact cards were applied:

- ***AUTOMATIC_SURFACE_TO_SURFACE**
- ***AUTOMATIC_SURFACE_TO_SURFACE_SMOOTH**
- ***AUTOMATIC_SURFACE_TO_SURFACE_MORTAR**
- ***AUTOMATIC_NODES_TO_SURFACE**
- ***AUTOMATIC_NODES_TO_SURFACE_SMOOTH**
- ***ONE_WAY_SURFACE_TO_SURFACE**
- ***ONE_WAY_SURFACE_TO_SURFACE_SMOOTH**
- ***ERODING_SURFACE_TO_SURFACE**
- ***ERODING_NODES_TO_SURFACE**

Regarding the self-contact of the aluminium specimen, ***AUTOMATIC_SINGLE_SURFACE** contact was employed for applications where damage was not considered. When damage was enabled, ***ERODING_SINGLE_SURFACE** was used. For all contact formulations, SOFT = 1 was used and a value of 0.3 was applied for FD and FS.

A solid element mesh with a characteristic length of 0.55 mm was used. The default formulation for solid elements ELFORM = 1 together with an hourglass control IHQ = 5 and QM = 0.03 was used.

A ***MAT_USER_DEFINED_MATERIAL_MODELS** material model was adopted to model material properties. Damage was disabled for models with ***AUTOMATIC** and ***ONE_WAY** contact types. In simulations where damage was of interest, such as models with ***ERODING** contact types, the CL damage criterion was used.

Fig.20 shows the force-displacement curves for the contact formulations used. All contacts display similar behaviour and a good agreement between them. According to Fig.20, the force curves appear to be invariant by the type of contact algorithm chosen. However, a slight difference can be observed when the ***SMOOTH** option is activated. From a displacement of 42 mm, all models with ***SMOOTH** contact types exhibit lower force values compared to the other contact formulations. However, no differences in the deformation patterns were observed.

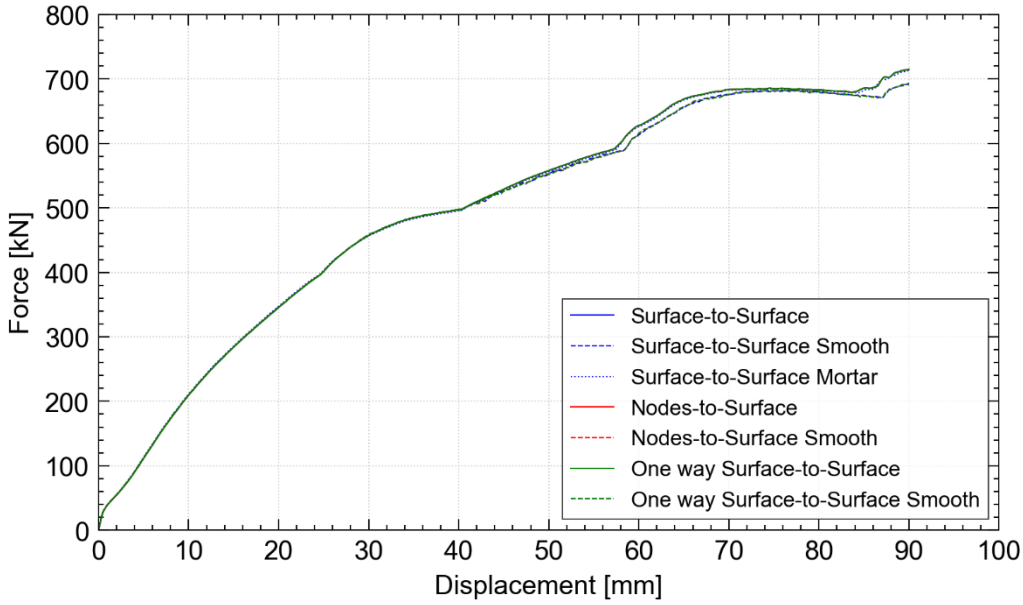


*Fig.20: Force-displacement curves for different contact formulations used in models in which damage is disabled.*

Fig.21 shows a comparison between force-displacement curves for the contact formulations used for models with damage and the corresponding contact formulations models where damage is not activated. It is observed that models with ***ERODING** contact types exhibit similar behaviour before damage occurs. Both ***ERODING** contact formulations predict a force drop at 46 mm of displacement caused by material failure. Similar curves are observed post-fracture. A second drop of force is captured at 64 mm, followed by a force peak at 74 mm. Comparing the ***ERODING** contact formulations, ***ERODING_SURFACE_TO_SURFACE** contact exhibits a slightly higher force peak.

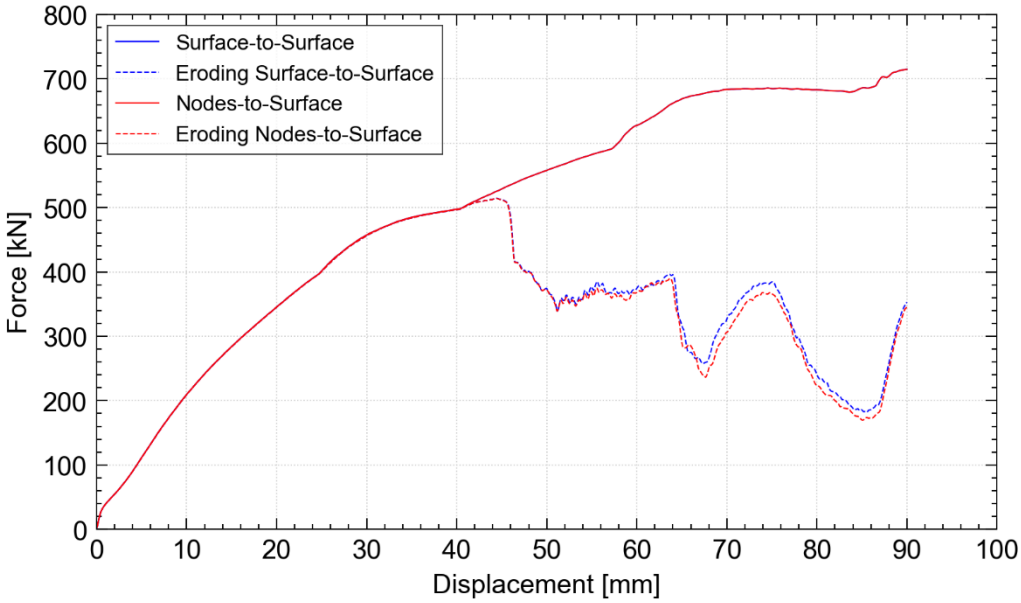


*Fig.21: Force-displacement curves for contact formulations.*

Table 3 shows the computational cost for each contact formulation applied. As expected, models with ***ERODING** contact types in which damage is enabled exhibit greater computational times. Reduced computational times were obtained for ***AUTOMATIC_SURFACE_TO_SURFACE, *AUTOMATIC_NODES_TO_SURFACE** and ***ONE_WAY_SURFACE_TO_SURFACE** contact formulations. These contact algorithms resulted in the most computationally effective formulations. From Table 3, it stands out that contacts with ***SMOOTH** option were 1.3 times more expensive. The ***AUTOMATIC_SURFACE_TO_SURFACE_SMOOTH** contact formulation was two times more costly, thus resulting in the most expensive contact algorithm for models without damage.

| Contact Formulation | CPU Time (hours) |
|---|---|
| ***AUTOMATIC_SURFACE_TO_SURFACE** | 6.3 |
| ***AUTOMATIC_SURFACE_TO_SURFACE_SMOOTH** | 13.7 |
| ***AUTOMATIC_SURFACE_TO_SURFACE_MORTAR** | 8.6 |
| ***AUTOMATIC_NODES_TO_SURFACE** | 6.2 |
| ***AUTOMATIC_NODES_TO_SURFACE_SMOOTH** | 9.3 |
| ***ONE_WAY_SURFACE_TO_SURFACE** | 6.2 |
| ***ONE_WAY_SURFACE_TO_SURFACE_SMOOTH** | 9.4 |
| ***ERODING_SURFACE_TO_SURFACE** | 28.4 |
| ***ERODING_NODES_TO_SURFACE** | 25.0 |

*Table 3: Computational cost of contact formulations. Models were simulated with 48 MPP processors.*

### *3.4.4 Friction coefficient*

The influence of the chosen friction coefficient on the numerical models was studied. The applied friction coefficient was varied from 0 to 0.3. The same values for both static and dynamic friction coefficients were implemented for all contact formulations. ***CONTACT_ERODING_SURFACE_TO_SURFACE** with SOFT = 1 was used to model the contact between different parts. To ensure self-contact, ***CONTACT_ERODING_SINGLE_SURFACE** with SOFT = 1 was applied.

Fig.22 shows the force-displacement curves for the different friction coefficients analysed. The results show a similar behaviour before the first crack appears. From the data in Fig.22, it is apparent that in simulations with friction, a first material fracture at 46 mm of displacement is predicted. In contrast, when a frictionless test is considered, the drop in force caused by the formation of the crack is predicted at a higher displacement. From the figure, it can be seen that higher friction coefficients lead to higher force levels after failure of the profile.

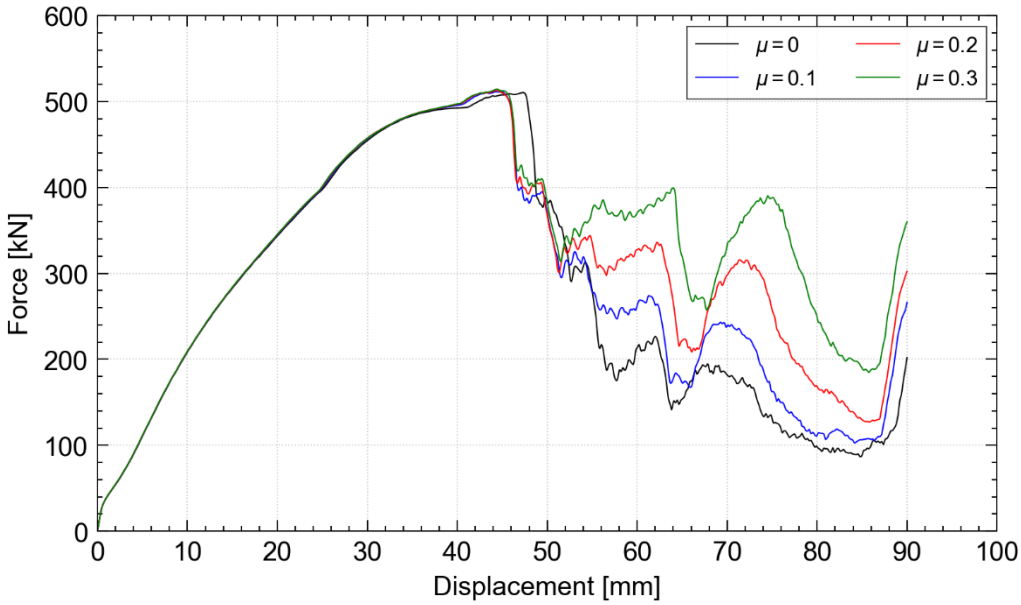


*Fig.22: Force-displacement curves for different friction coefficients applied.*

## 4 Summary

The numerical modelling of a thick-walled aluminium extrusion to protect battery trays in electric vehicles was studied. Material properties of four commonly used aluminium alloys intended for energy absorption applications were calibrated from uniaxial tensile tests.

Solid and shell elements exhibited significant differences when modelling a pole-crushing test on a thick-walled profile. Shell models proved to predict notably lower force values compared to a solid model. Also, differences in the deformation mode were observed between solid and shell models. When a damage model was included, shell models predicted failure earlier compared to solid models. Furthermore, solid and shell models exhibited differences in the failure mode.

The value of $\phi$ in the Extended Cockcroft-Latham model demonstrated to play a major role on material failure for thick-walled aluminium extrusions. Reducing the value of $\phi$ led to the occurrence of out-of-plane shear cracks, as $\phi$ controls the shear ductility.

Regarding the element formulation, selecting an ELFORM = 1 for a refined mesh resulted in a reasonable balance between accuracy and computational cost.

No significant differences in terms of accuracy were observed for the contact formulations. However, enabling the **`*SMOOTH`** option increased by more than 1.3 times the computational cost of the numerical model.

The friction coefficient was shown to have a significant influence when modelling a pole-crushing test. Major differences in the computed force were observed between low and high-friction models after failure of the profile. Therefore, a correct friction coefficient is crucial to obtain accurate results.

## 5 Literature

[1] G. Sun, M. Deng, G. Zheng, and Q. Li, ‘Design for cost performance of crashworthy structures made of high strength steel’, *Thin-Walled Struct.*, 2019, 458–472.

[2] M. Langseth, O. S. Hopperstad, and T. Berstad, 'Crashworthiness of aluminium extrusions: validation of numerical simulation, effect of mass ratio and impact velocity', *Int. J. Impact Eng.*, 9–10, 1999, 829–854.
[3] T. Pang, G. Zheng, J. Fang, D. Ruan, and G. Sun, 'Energy absorption mechanism of axially-varying thickness (AVT) multicell thin-walled structures under out-of-plane loading', *Eng. Struct.*, 2019, 109130.
[4] F. Barlat *et al.*, 'Yield function development for aluminum alloy sheets', *J. Mech. Phys. Solids*, 11–12, 1997, 1727–1763.
[5] G. Gruben, O. S. Hopperstad, and T. Børvik, 'Evaluation of uncoupled ductile fracture criteria for the dual-phase steel Docol 600DL', *Int. J. Mech. Sci.*, 1, 2012, 133–146.
[6] M. Costas, D. Morin, O. S. Hopperstad, T. Børvik, and M. Langseth, 'A through-thickness damage regularisation scheme for shell elements subjected to severe bending and membrane deformations', *J. Mech. Phys. Solids*, 2019, 190–206.
[7] J. K. Holmen, J. Johnsen, D. Morin, T. Børvik, and M. Langseth, 'Application of *MAT_258 for Bending and Crushing of Extruded Aluminum Profiles Using Shell Elements', 16th International LS-DYNA Users Conference, Detroit, USA, 2020.
[8] Livermore Software Technology Corporation (LSTC), 'LS-DYNA Keyword User's Manual'. 2021.
[9] Livermore Software Technology Corporation (LSTC), 'LS-OPT User's Manual, version 6.0'. 2019.